Simulating human sleep spindle MEG and EEG from ion channel and circuit level dynamics

Rosen[1,*], B.Q., Krishnan[2,*] G.P., Sanda[2], P., Komarov[2], M., Sejnowski[1,3], T., Rulkov[4], N., Bazhenov[1,2,^] ,M., Halgren[1,5,6,^], E.
*co-first ^co-senior

1. Neurosciences Graduate Program, University of Californa, San Diego, La Jolla CA
2. Department of Medicine, University of California, San Diego, La Jolla CA
3. The Salk Institute, La Jolla CA
4. BioCiruits Institute, University of California, San Diego, La Jolla CA
5. Department of Radiology, University of California, San Diego, La Jolla CA
6. Department of Neurosciences, University of California, San Diego, La Jolla CA

Abstract

Although they form a unitary phenomenon, the relationship between extracranial MEG/EEG and transmembrane ion flows is understood only as a general principle rather than as a well-articulated and quantified causal chain. Here we present an integrated multiscale model, consisting of a neural simulation of the thalamus and cortex during stage N2 non-REM sleep and a biophysical model projecting cortical current density to MEG/EEG fields. The network model generated sleep spindles using interactions of local and distant network connections and intrinsic currents within thalamocortical circuits, as specified based on our previous work. 32,652 cortical neurons were mapped onto the cortical surface reconstructed from each subject's structural MRI, and they were interconnected based on cortical geodesic distances. MRIs were used to generate a boundary element method (BEM) quasi-electrostatic model enabling simulated cortical activity during spindles to be projected to the MEG/EEG sensors. Dipole amplitudes were based on laminar recordings in humans. The resulting simulated spindles were found to be similar in amplitude and topography to empirical examples in the same subjects. Spindles modeled as originating in core and matrix thalamocortical systems were more similar to spindles recorded with MEG and EEG, respectively, then *vice versa*. This multiscale model provides a platform for the principled quantitative integration of existing information relevant to the generation of sleep spindles, and allows the implications of future findings to be explored. It provides a proof of principle for a methodological framework allowing large-scale integrative brain oscillations to be understood in terms of their underlying channels and synapses.

Keywords
MEG, EEG, Forward Model, Sleep, Spindle, Thalamocortical

Introduction

Magnetoencephalography (MEG) and electroencephalography (EEG, together M/EEG), are complementary, non-invasive, instantaneous, and, in the later case, inexpensive and clinically essential, measures of human neural activity. M/EEG are measured as global brain activities, but are known to ultimately arise from channel currents, at a spatial scale ~9 orders of magnitude smaller (Cohen, 2017). The causal chain which leads to M/EEG can be divided into two linked domains: (1) the biophysical propagation of electromagnetic fields after summating and cancelling under anatomical constraints; and (2) the neurobiology of large networks of active neurons whose ionic currents generate these fields. Here we present an initial effort to traverse the spatial scales by integrating simulations of large networks of neurons with biophysical models of electromagnetic propagation, informed by non-invasive imaging and invasive recordings in humans, as well as decades of work in animal models.

Ligand- and voltage-gated transmembrane currents are created by the interaction between the intrinsic channel properties of each neurons and the activity of the network. These currents flow through intracellular and extracellular spaces to form complete circuits, restricted by cellular membranes, and thus microscopic cellular anatomy (Einevoll et al., 2013). Currents cancel and summate locally with those of other neurons in the same cortical column, producing a net current which can be expressed as a multipole expansion (Nunez and Srinivasan, 2009). At a distance, the dipolar term predominates, and the local contribution is typically expressed as an 'equivalent current dipole' (ECD). Before reaching the sensors, ECDs from different columns cancel and summate mesoscopically with other columns depending on their relative position and orientation in the highly folded cortical surface, and the covariance and phase synchrony of their magnitudes over time (Ahlfors et al., 2010a, 2010b; Irimia et al., 2012; Linden et al., 2011). Ultimately, the signal at each M/EEG sensor is the result of the complex cancellation and summation of microscopic synaptic and intrinsic currents from the many thousands or millions of neurons contributing to any single sensor's leadfield.

Transmembrane currents are the result of spontaneous or evoked neural activity, which can be modeled computationally with various degrees of realism, balancing accuracy at the individual cell level against the quantity of neurons that comprise the simulated network. In the current study, we focus on a model for stage 2 of non-rapid eye movement sleep (N2) which generates spontaneous sleep spindles. Sleep spindles manifest in normal M/EEG as spontaneous bursts of 10-16 Hz activity lasting 0.5-2 s in and are thought to be important for memory consolidation (Andrillon et al., 2011; Bonjean et al., 2011; Contreras et al., 1996; Dehghani et al., 2011; Diekelmann and Born, 2010; Sejnowski and Destexhe, 2000). A large number of studies in animal models have established the key elements in spindle generation: local circuit interactions between thalamo-cortical projection and thalamic reticular nucleus neurons, reinforcing intrinsic rhythmicity from successive activation of the hyperpolarization-activated cation current, I_h (Destexhe et al., 1996; McCormick and Pape, 1990) and low-threshold Ca^{2+} current I_T (Huguenard and McCormick, 1992; Huguenard and Prince, 1992). Secondarily, the long loop return from the cortex may play a role in synchronizing and terminating the spindle (Bonjean et al., 2011).

Although the initial circuitry and cellular properties generating spindles are thus in the thalamus, the transmembrane currents that produce the M/EEG are cortical. The thalamocortical projection connecting these structures is comprised of a focal projection to layer 4 (termed the 'core'), and a distributed projection to upper layers (termed the 'matrix') (Jones, 2002, 2001). We found previously that sleep spindles detected in MEG are more numerous and less synchronous than EEG spindles (Dehghani et al., 2011, 2010), and suggested that this may reflect a relatively greater sensitivity of EEG to the matrix and MEG to the core projections (Piantoni et al., 2016). Consistent data has been obtained with laminar recordings showing primary involvement of middle or upper layers in different spindles or parts of spindles (Hagler et al., in press).

In this report we combine neural and biophysical models to generate M/EEG sleep spindles. The neural model is based on our previous computational modeling including the thalamic and cortical local and distant circuits involved in spindles, including matrix and core (Bonjean et al., 2012; Krishnan et al., 2017, 2016). All relevant thalamic ligand- and voltage-gated currents are included. The cortical elements are mapped to 20,484 locations on the ~1 mm resolution cortical surface reconstructed from structural MRI. We have found in previous simulations that this resolution is necessary in order to accurately model the interactions between simultaneously active ECDs in producing M/EEG signals (Ahlfors et al., 2010b). In order to computationally model this large number of elements, it was necessary to use 'MAP' neurons, which simulate individual cell dynamics using differential equations (Rulkov, N.F., Timofeev, I., Bazhenov, 2004).

Empirical sleep M/EEG and structural MRI were collected to provide a basis for model evaluation and donor cortical and cranial substrates in which to embed simulated neurons. In our framework, the neural activity of individual persons is modeled, as connections among neurons are derived in part from the cortical geometry of the subject against whose data the model will be compared. Microscopic cellular currents are scaled to mesoscopic equivalent dipoles using factors derived from human laminar electrode data. The extracranial electromagnetic fields generated by these mesoscopic sources are derived by quasi-electrostatic forward modeling, which accounts for orientation induced summation and cancelation by utilizing high-resolution cortical and cranial geometry. Simulated macroscale extracranial M/EEG fields are compared to empirical non-invasive datasets by means of their topography and amplitude.

The modeling approach employed here, an extension of our earlier work, allows for the currents of the coupled core and matrix networks to be isolated and the relative contributions of these isolates to MEG and EEG, respectively, to be estimated. We find that the topography and spatiotemporal patterns of matrix-derived EEG and core-derived MEG better match empirical data than the reverse. More generally, we demonstrate a proof-of-concept for relating microscale neuronal parameters to macroscale M/EEG observations.

Materials and Methods

Overview

The overall structure of the study is shown in Fig. 1. Two kinds of models were constructed: a Neural Model to compute sleep spindle activity during N2 sleep, based on the known anatomy and physiology of the thalamus and cortex; and a Biophysical Model to project the activity to the M/EEG sensors. Empirical Measurements were obtained and analyzed to produce Derived Measures, used to specify the models and validate the model: Structural MRI to define the location and orientation of cortical generating dipoles; Laminar recordings to define the strength of the Equivalent Current Dipoles generating spindles; ECoG to modulate the strength in different areas as observed in cortical recordings; and M/EEG in the same subjects to permit validation of model predictions of amplitude, topography and covariance.

Empirical Data

Participants: Structural MRI, MEG and EEG data were record for 3 healthy adults (S1, S2, S3) in the supine position. Two subjects were men. Written informed consent approved by the institutional review board of the University of Californa, San Diego was obtained for all subjects. A whole-head MEG system with integrated EEG cap (Elekta Neuromag) was used to collect 204 planar gradiometers and 60 EEG channels. EEG data were referenced to the left mastoid. The position of the subjects' head within the MEG helmet was monitored using head position indicator (HPI) coils, updated every 15-20 minutes. Each subjects headshape, HPI coil locations, and and EEG electrode positions were digitized (Polhemus isotrak). Structural MR images were acquired in a separate session.

MEG/EEG: MEG/EEG data were acquired during natural sleep in the supine position at 1 kHz with a 300 Hz low-pass antialiasing filter. Epochs of stage II non-REM sleep were selected for analysis using standard criteria (Iber et al., 2007). Channels with poor data quality or gross artifacts were excluded by visual inspection. The electrocardiogram artifact was removed with independent component analysis (Delorme and Makeig, 2004). Clean data were band-pass filtered to between 10 and 16 Hz.

Structural MRI: High-resolution structural images were acquired with a 1.5 Signa HDx whole body scanner (General Electric). The acquisition protocol consisted of a 3-plane localizer, calibration scan, and a high-resolution T1-weighted MP-RAGE scans (TR = 10.728 s, TE = 4.872 ms, TI = 1000 ms, flip angle = 8 degrees, FOV = 256, 176 sagittal slices, 1 mm isotropic).

Laminar recordings: As described in detail in (Hagler et al., in press), laminar microelectrodes arrays (Ulbert et al., 2001) were implanted into cortical tissue designated for resection in 5 patients undergoing surgical treatment for drug resistant epilepsy. These arrays consisted of twenty-four 0.040 mm diameter contacts with 0.150 mm on-center spacing and were inserted along the surface normal of the cortex. Bipolar referencing of reported laminar potentials yields a depth-resolved measure of potential gradients within and among cortical layers to be recorded simultaneously.

Derived Measures

Calculation of equivalent current dipole (ECD) strength. The laminar current source density (CSD) of sleep spindles was calculated by estimating the explicit quasi-electrostatic inverse of the laminar potential gradients (Pettersen et al., 2006). The spindle ECD of the probed cortical column was then computed by computing the volume integral of CSD. We found sleep spindle surface current densities have an average maximum analytic amplitude of ~0.03 nAm/mm^2. Therefore, the arbitrarily scaled simulated neural currents (in nA) were scaled to match in amplitude this surface current density. These surface current densities (in nAm/mm^2) were multiplied by the approximate Voronoi area (Meyer et al., 2003) of the cortical patch each represents, yielding corresponding ECD amplitudes in nAm.

Covariance: The covariance among the M/EEG sensors was computed in sliding 1-second windows with 50% overlap over a 10 second period. The variance-covariance matrices of all windows were then averaged to yield mean covariance matrices. Empirical and simulated covariance were quantitatively compared using correlation matrix distance (CMD) (Herdin et al., 2005), a scale insensitive metric varying between 0 (identical) and 1 (maximally different). The Hilbert transform was used to extract the 10-16 Hz analytic signal and topographic maps of sensor activity were generated by averaging the analytic signal modulus (or narrow-band envelope) across time and interpolating this data over flattened sensor positions (Oostenveld et al., 2011).

Biophysical model

Cortical reconstruction: White-gray matter surfaces were reconstructed from the MR volumes using FreeSurfer (Fischl, 2012). Surfaces were sampled at three resolutions as recursively subdivided icosahedra with 642, 10,242, and 163,842 vertices per hemisphere, wherein lower resolution meshes are nested subsets of higher resolution meshes. These are referred to as ico3, ico5, and ico7 surfaces, respectively, indicating the number of subdivisions. Within each hemisphere the geodesic distance between all pairs of vertices was computed using the Dijkstra approximation (Balasubramanian et al., 2009) with 13 Steiner nodes.

Forward Model (ECDs to M/EEG): The forward model, or gain matrix describing the gradiometer and EEG sensor activity produced by each equivalent dipole was then computed for each subject's cortex. In addition to the white-gray matter surface, four extra-cortical boundary shells were reconstructed from the segmented (Fischl, 2012) images: gray-matter-cerebral-spinal fluid (CSF), CSF-inner skull, inner skull-outer skull, and outer skull-scalp. While the cranial boundaries consisted of triangular meshes with 5,124 vertices, critically, the cortical mesh was sampled at ~1 mm resolution (327,684 vertices) in order to capture the summation and cancelation of opposed dipoles. The position of these surfaces relative to the EEG sensors and HPI coils was determined by registering the digitized headshape to the outer-scalp surface using non-linear optimization (matlab's fmincon) with manual corrections. The position of these surfaces relative to the gradiometers was computed using the known relative positions between and the surfaces and the HPI coils, and the HPI coils and the gradiometers. The orientation of each dipole was set to the surface normal of the white-gray interface. The quasi-electrostatic forward solution was numerically computed using a four shell

boundary element model, or BEM (Gramfort et al., 2010) , with conductivities of 0.33, 0.0042, 0.011, and 0.33 S/m, for the brain, CSF, skull, and scalp, respectively. Simulated EEG and MEG gradiometer time series were generated independently for core and matrix system pyramidal neurons and then subjected to the same analyses as the empirical data, described above.

Neural model

Neurons: We used a computational model of a thalamocortical network (Fig 2A) with three layers in cortex, with each layer comprising of excitatory (PY) neurons and inhibitory (IN) neurons. The thalamus consisted of a network of core (specific) and matrix (non-specific) nuclei, each consisting of thalamic relay (TC) and reticular (RE) neurons. A computationally efficient phenomenological model based on difference equation (map-based) model was used for cortical PY and IN cells. We have previously demonstrated that such a map based neuron is computationally efficient and able to reproduce the same response characteristics of conductance based neurons (Bazhenov et al., 2008; Rulkov, N.F., Timofeev, I., Bazhenov, 2004; Rulkov and Bazhenov, 2008) and also capable of generating sleep oscillations (Komarov et al., 2017). The following equation describes the update of the PY neurons in time:

$$x_{t+1} = f_\alpha\left(x_t\,,\ y_t + \beta I_{syn}\right)$$

$$y_{t+1} = y_t - \mu(x_t + 1) + \mu\,\sigma + \mu * \beta_y I_{syn} \qquad [1]$$

where variable x_t represents the membrane potential of a biological neuron at time t and y_t represent slow varying ion channel dynamics. The parameter μ (=0.0005) describes the change in the slow variable (μ less than 1 lead to slow update of y variable). The parameter β scale the input synaptic currents (I_{syn}) for x variable, with β =0.133. The parameter σ (=0.02) defines the resting potential of the model neuron. The function f_α is given below:

$$f_\alpha\,(x_t, u_t) = \begin{cases} \frac{\alpha}{1-x_t} + u_t, & x \le 0 \\ \alpha + u_t, & 0 < x_t < \alpha + u_t \ \ x_{t-1} \le 0 \\ -1, & x_t \ge \alpha + u_t \ OR\ x_{t-1} > 0 \end{cases} \qquad [2]$$

where u_t is taken as $y_t + \beta\ I_{syn}$ from Eq 1, α (=3.65) is a control parameter which was set to obtain tonic spiking like activity for wide range of input currents. The inhibitory neurons were implemented using only the x variable to capture the fast spiking nature of inhibitory neurons and is described by the following equation:

$$x_{t+1} = f_\alpha\left(x_t\,, y^* + \beta\ I_{syn}\right) \qquad [3]$$

where, y^*=-2.90 with the same f_α function as Eq 2 with α =3.8 and β =0.05.

The thalamic TC and RE cells were modeled as conductance based neurons, described by the following equation:

$$C_m \frac{dV}{dt} = -\,g_{leak}\left(V - E_{leak}\right) - I_{int} - I_{syn} \qquad [4]$$

where the membrane capacitance, C_m, is equal to 1 μF/cm^2, non-specific (mixed Na^+ and

Cl^-) leakage conductance, g_{leak}, is equal to 0.0142 mS/cm^2 for TC cells and 0.05 mS/cm^2 for RE cells, and the reversal potential, E_{leak}, is equal to -70 mV for TC cells and -77 mV for RE cells. I_{int} is the sum of active intrinsic currents, and I_{syn} is the sum of synaptic currents. The area of a RE cell and a TC cell was 1.43x10^{-4} cm^2 and 2.9x10^{-4} cm^2, respectively. RE and TC cells included fast sodium current, I_{Na}, a fast potassium current, I_K, a low-threshold Ca^{2+} current I_T, and a potassium leak current, $I_{KL} = g_{KL}$ (V - E_{KL}), where E_{KL} = -95 mV. In addition, a hyperpolarization-activated cation current, I_h, was also included in TC cells. For TC cells, the maximal conductances are g_K = 10 mS/cm^2, g_{Na}= 90 mS/cm^2, g_T= 2.2 mS/cm^2, g_h = 0.017 mS/cm^2, g_{KL} = 0.0142 mS/cm^2. For RE cells, the maximal conductances are g_K = 10 mS/cm^2, g_{Na} = 100 mS/cm^2, g_T = 2.3 mS/cm^2, g_{leak} = 0.005 mS/cm^2.The expressions of voltage- and Ca^{2+}- dependent transition rates for all currents are given in (Bazhenov et al., 2002; Chen et al., 2012).

Synaptic currents: All the inputs to the map based neurons were described by the

$$\{g_{t+1}^{syn}, d_{t+1}\} = \begin{cases} \{\gamma g_t^{syn} + g_{syn} d_n, (1-\eta) d_n\}, & spike_{pre} \\ \{\gamma g_t^{syn}, \ 1-(1-\delta)(1-d_n)\},, & otherwise \end{cases} \quad [5]$$

where g_{t+1}^{syn} and d_{t+1} are the synaptic conductance and depression variable for time t+1, $g_{syn}$is the synaptic coupling strength similar to the maximal conductance. The parameter $\gamma = 0.99$ is the decay variable to capture the first order kinetics of the synaptic transmission, $\eta = 0.00005$ is the rate of decay of the depression variable (d). The synaptic currents that are input to all conductance based neurons were described as:

$$\mathrm{I_{syn}} = g_{syn}[O](V - E_{syn}) \quad [6]$$

where $g_{syn}$is the maximal conductance, $[O]$ is the fraction of open channels, and E_{syn} is the reversal potential. In RE and PY cells, reversal potential was 0 mV for AMPA receptors, and -70 mV for GABA-A receptors. For TC cells, the reversal potential was -80 mV for GABA-A receptors, and -95 mV for GABA-B receptors. GABAA, and AMPA synaptic currents were modeled by the first-order activation schemes. GABA-B receptors were modeled by a higher-order reaction scheme that considers the activation of K^+ channels by G-proteins. The equations for all synaptic currents were given in (Timofeev, I., Grenier F., Bazhenov, M., Sejnowski, T.J., Steriade, 2000).

Spontaneous miniature EPSPs and IPSPs were included for the AMPA and GABA-A connections within cortical neurons. The arrival times of miniature EPSPs and IPSPs followed the Poisson process (Stevens, 1993), with time-dependent mean rate $\mu = \log(\frac{t-t_0+T}{T})$ where t is current time and t_0 was timing of the last presynaptic spike and T=50ms.

Synaptic conductance: A detailed network connectivity is shown in Fig 2A. The maximal conductances for various connections were $g_{GABA\text{-}A}$(RE-TC) = 0.045 μS, $g_{GABA\text{-}B}$(RE-TC) = 0.06 μS, $g_{GABA\text{-}A}$(RE-RE) = 0.175 μS; core thalamus: g_{AMPA}(TC-PY) = 0.03 μS, g_{AMPA}(TC-IN) = 0.015 μS; matrix thalamus: g_{AMPA}(TC-PY) = 0.045 μS, g_{AMPA}(TC-IN) = 0.02 μS; connections within each layer (matrix, core and L6) pyramidal neurnons: g_{AMPA}(PY-PY) = 2.5 nS, g_{NMDA}(PY-PY) = 0.4 nS; connection from matrix to core: g_{AMPA}(PY-PY) = 1.5 nS, g_{NMDA}(PY-PY) = 0.1 nS; connection from matrix to L6 :

g_{AMPA}(PY-PY) = 2.0 nS, gNMDA(PY-PY) = 0.2 nS; connection from core to matrix: g_{AMPA} (PY-PY) = 1.5 nS, g_{NMDA}(PY-PY) = 0.1 nS; connection from core to L6: g_{AMPA}(PY-PY) = 2.0 nS, g_{NMDA}(PY-PY) = 0.2 nS; connection from L6 to matrix: g_{AMPA}(PY-PY) = 2.0 nS, g_{NMDA}(PY-PY) = 0.2 nS; connection from L6 to core: g_{AMPA}(PY-PY) = 1.5 nS, gNMDA(PY-PY) = 0.1 nS; connection betwen PY and IN cells for all layers: g_{AMPA}(PY-IN) = 0.05 μS, g_{NMDA}(PY-IN) = 0.4 nS, g_{GABA-A}(IN-PY) = 0.05 μS and connection from core and L6 cells to thalamic neurons: g_{AMPA}(PY-TC) = 0.025 μS, g_{AMPA}(PY-RE) = 0.045 μS.

Network connectivity: For each subject's donor cortex, one pyramidal neuron was simulated for each vertex in the ico5 mesh (10,242 vertices per hemisphere) for each of layers matrix, core, and L6. The ico3 mesh was populated with inhibitory and thalamic neurons at each of 642 vertices per hemisphere. For all intra-hemispheric synapses, connectively was established by comparing synapse-specific fan-out radii to the geodesic distance between vertices on the ico7 cortex (163,842 vertices per hemisphere), see Fig. 2B. Inter-hemispheric synapses were threaded between homologously located neurons in 85% of cases and the remaining connections were made between randomly located neurons. Fig. 3B shows simulated current on an inflated cortex at a single time point for the core and matrix neurons.

Results

We designed a thalamocortical network model that combined the detailed laminar connectivity with the network connectivity of the whole brain based on MRI reconstructions. Using this approach we demonstrate the feasibility of connecting the cellular level activity with the macroscopic activity seen in EEG/MEG. We used a difference equation or map-based model for cortical neurons, which has low computational cost requires for simulating large-scale networks and conductance based neuronal models for thalamic network, as required to model specific patterns of electrical activity.

The state of the network was set to be stage 2 sleep state by modifying the intrinsic and synaptic currents to mimic the level of low acetylcholine, nor-epinephrine and histamine similar to our previous work. In this state, the network spontaneously generated electrical activity similar to our previous studies (Bazhenov et al., 2000; Bonjean et al., 2011; Krishnan et al., 2016) consisting of multiple randomly occurring spindle events involving thalamic and cortical neuronal populations. The cortical and thalamic neurons in both the core and matrix system had elevated and synchronized firing, during such spindle events (Fig 3A) consistent with previous in-vivo experimental recordings (Steriade et al., 1993). Next, we applied a forward modeling technique that used results from the large-scale simulations of thalamocortical network to simulate EEG and MEG signals.

Microscopic transmembrane currents were scaled up to mesoscopic patch current densities, a quantity corresponding to the dipole moment per unit volume, or equivalent current dipole (ECD). This was accomplished by in two steps: scaling the transmembrane currents to match empirical spindle ECDs recorded from human laminar microelectrode data, and scaling these current densities to the cortical patch area represented by each

neuron, as described below.

We found, that the model was able to simulate the essential elements of empirical MEG/EEG. The topographies of simulated and experimental data for S1 are shown in fig. 4A. Simulated topographies are qualitatively similar to experimental ones. Thus, the matrix EEG and core MEG topographies better matched the empirical topographies than *vice versa.* The models also replicated the approximate absolute magnitude of the M/EEG signal.

In addition to gross topography, the model reproduced the multivariate spatial-temporal structure of empirical MEG/EEG. The empirical and simulated 10-16 Hz covariance matrices for S1 are shown in fig. 4A. The correlation matrix distance (CMD) (Herdin et al., 2005) between the variance-covariance matrices of empirical M/EEG and simulated M/EEG are shown in table 1. Mean distances for core MEG, matrix MEG, core EEG, and matrix EEG ($p = 0.0420$, $p = 0.427$, $p = 5.190e\text{-}4$, $p = 0.0023$) were all less than for maximally different matrices. The distances were particularly small, indicating a close match, for EEG. Simulated core MEG covariance was more similar to empirical MEG covariance than matrix covariance (mean CMD = 0.4263 vs. 0.4533, $p = 0.0428$). In contrast, matrix covariance was more similar to empirical EEG covariance (mean CMD = 0.1843 vs. 0.0999, $p = 0.1534$). These data support the hypothesis that EEG is more sensitive the matrix system neurons of the matrix and that MEG gradiometers are more sensitive to the core system neurons of the core system.

Discussion

In this study, we developed a computationally efficient large-scale hybrid thalamocortical model of sleep spindles with cortical patches that were realistically arranged in space based on the structural MRI data. Using the output of the model simulation, we obtained the activity seen in EEG and MEG sensors. The spatial and temporal features of MEG/EEG derived from the model were similar to those found in our empirical results thereby validating our approach. In addition, we confirmed the previous hypothesis (Bonjean et al., 2011; Dehghani et al., 2010) that MEG activity during spindle reflects the activity of the superficial matrix layers while EEG is more sensitive to core neurons. Thus, using this approach, we demonstrate the viability of an integrated model for the generation of EEG/MEG, proceeding from ionic and synaptic activity, through local and distant networks, whose currents are then passed through a realistic biophysical model to generate MEEG fields that correspond to empirical recordings, a foundational problem in neuroimaging.

At its base, our study used a detailed 'Hodgkin-Huxley' model to simulate EEG/MEG. Ritter et al. (Ritter et al., 2013) have demonstrated modeled EEG signals from population based neural mass models of cortical activity projected to extracranial sensors. While such models could reproduce the spectrogram of EEG, they do not explicitly resolve activity at the level of individual neuron's ionic or synaptic currents. This becomes critical when trying to leverage information from extensive intracellular and direct recordings of cortical and thalamic activity, e.g. (Steriade and Timofeev, 2003). Costa and colleagues (Costa et al., 2016) included some of these details in their neural mass

model, but their biophysical modeling of EEG was rudimentary, only considering an anatomically and physiologically implausible point source.

Extracranial MEG/EEG fields generated by a MEG/EEG dipole depend not only on its amplitude, but are also highly dependent on the extent of spatial-temporal synchrony across the cortex (or patch size), and the orientations of a given and the other dipoles (Ahlfors et al., 2010a; Lutkenhoner, 2003). Dipoles are created by the post-synaptic currents of pyramidal neurons aligned and are thus perpendicular to cortical surface (Lopes Da Silva, 2004; Nunez and Srinivasan, 2009). Thus, synchronous dipoles with opposed orientations, such as those on opposite side of the sulcal walls, will cancel each other out. If fact, the majority of the typical MEG signal is canceled because of this phenomena (Ahlfors et al., 2010b; Lutkenhoner, 2003). Therefore, computing the electrostatic forward solution for a high-resolution cortical mesh is critical for capturing the effects of dipole cancelation and summation. Indeed, our surface geometry was sampled at ~1 mm resolution or 327,684 sources.

The leadfields of MEG gradiometers are smaller than those of EEG, even though MEG sensors are typically further away from the scalp (Irimia et al., 2012). This is primarily because EEG is smeared by the skull and cranial tissues whereas MEG these structures are mostly transparent to MEG (Hämäläinen and Ilmoniemi, 1994) and also because the sources of bipolar gradients, such as MEG gradiometers are more focal than distantly reference scalp EEG. It is likely that intermodal differences in leadfield extent render the instruments differentially sensitive to phenomena with broad or focal spatial extents (Dehghani et al., 2010). The core and matrix thalamocortical pathways (Jones, 2002, 2001), which innervate subgranular neurons sparsely and superical neurons broadly, respectively, can explain differences in the spatial extent of MEG and EEG spindles by attributing the MEG activity to the core and EEG activity to the matrix (Bonjean et al., 2012). In this study we confirm this prediction by deriving the EEG and MEG activity from a multi-layer cortical network that includes the thalamus. We found that derived MEG activity reflects the core while that of EEG reflects synaptic inputs of the matrix.

Given the scale and complexity of the system that our framework attempts to emulate, it unsurprising that its limitations are numerous. Most notably, this model does not take into account functional specialization or cytoarchitectonic differentiation among cortical regions. Future developments of our approach will incorporate structural and functional connectivity maps and parcellation, e.g. (Smith et al., 2013; van den Heuvel and Sporns, 2013).The scaling from single neuron current to patch ECD, while empirically grounded, is approximate in magnitude and restrictive in orientation. Subcortical areas other than the thalamus are not included in the models. While the direct contribution of these areas to extracranial M/EEG is minimal (Cohen et al., 2011), many, e.g. the nucleus basalis and hippocampus, may inform cortical activity during spindling. Future iterations will address these limitations.

A more comprehensive understanding of the relationship between neurochemistry, local field potentials, and non-invasive M/EEG might plausibly improve the diagnostic power of the latter techniques. Understanding the forward model from ion channel dynamics to M/EEG is the first step towards developing a principled inverse solution that maps M/EEG responses to clinically and physiologically relevant human *in vivo* molecular

measures.

References

Ahlfors, S.P., Han, J., Belliveau, J.W., Hämäläinen, M.S., 2010a. Sensitivity of MEG and EEG to source orientation. Brain Topogr. 23, 227–232. https://doi.org/10.1007/s10548-010-0154-x

Ahlfors, S.P., Han, J., Lin, F.H., Witzel, T., Belliveau, J.W., Hämäläinen, M.S., Halgren, E., 2010b. Cancellation of EEG and MEG signals generated by extended and distributed sources. Hum. Brain Mapp. 31, 140–149. https://doi.org/10.1002/hbm.20851

Andrillon, T., Nir, Y., Staba, R.J., Ferrarelli, F., Cirelli, C., Tononi, G., Fried, I., 2011. Sleep Spindles in Humans: Insights from Intracranial EEG and Unit Recordings. J. Neurosci. 31, 17821–17834. https://doi.org/10.1523/JNEUROSCI.2604-11.2011

Balasubramanian, M., Polimeni, J.R., Schwartz, E.L., 2009. Exact geodesics and shortest paths on polyhedral surfaces. IEEE Trans. Pattern Anal. Mach. Intell. 31, 1006–1016. https://doi.org/10.1109/TPAMI.2008.213

Bazhenov, M., Rulkov, N.F., Timofeev, I., 2008. Effect of synaptic connectivity on long-range synchronization of fast cortical oscillations. J. Neurophysiol. 100, 1562–1575. https://doi.org/10.1152/jn.90613.2008

Bazhenov, M., Timofeev, I., Steriade, M., Sejnowski, T., 2000. Spiking-bursting activity in the thalamic reticular nucleus initiates sequences of spindle oscillations in thalamic networks. J. Neurophysiol. 84, 1076–1087.

Bazhenov, M., Timofeev, I., Steriade, M., Sejnowski, T.J., 2002. Model of thalamocortical slow-wave sleep oscillations and transitions to activated States. J. Neurosci. 22, 8691–8704. https://doi.org/22/19/8691 [pii]

Bonjean, M., Baker, T., Bazhenov, M., Cash, S., Halgren, E., Sejnowski, T., 2012. Interactions between Core and Matrix Thalamocortical Projections in Human Sleep Spindle Synchronization. J. Neurosci. 32, 5250–5263. https://doi.org/10.1523/JNEUROSCI.6141-11.2012

Bonjean, M., Baker, T., Lemieux, M., Timofeev, I., Sejnowski, T., Bazhenov, M., 2011. Corticothalamic Feedback Controls Sleep Spindle Duration In Vivo. J. Neurosci. 31, 9124–9134. https://doi.org/10.1523/JNEUROSCI.0077-11.2011

Chen, J.-Y., Chauvette, S., Skorheim, S., Timofeev, I., Bazhenov, M., 2012. Interneuron-mediated inhibition synchronizes neuronal activity during slow oscillation. J. Physiol. 590, 3987–4010. https://doi.org/10.1113/jphysiol.2012.227462

Cohen, M.X., 2017. Where Does EEG Come From and What Does It Mean? Trends Neurosci. 40, 208–218. https://doi.org/10.1016/j.tins.2017.02.004

Cohen, M.X., Cavanagh, J.F., Slagter, H.A., 2011. Event-related potential activity in the basal ganglia differentiates rewards from nonrewards: Temporospatial principal components analysis and source localization of the feedback negativity: Commentary. Hum. Brain Mapp. 32, 2270–2271. https://doi.org/10.1002/hbm.21358

Contreras, D., Destexhe, A., Sejnowski, T.J., Steriade, M., 1996. Control of spatiotemporal coherence of a thalamic oscillation by corticothalamic feedback. Science (80-.). 274, 771–774. https://doi.org/10.1126/science.274.5288.771

Costa, M.S., Weigenand, A., Ngo, H.V. V, Marshall, L., Born, J., Martinetz, T.,

Claussen, J.C., 2016. A Thalamocortical Neural Mass Model of the EEG during NREM Sleep and Its Response to Auditory Stimulation. PLoS Comput. Biol. 12, 1–20. https://doi.org/10.1371/journal.pcbi.1005022

Dehghani, N., Cash, S.S., Halgren, E., 2011. Emergence of synchronous EEG spindles from asynchronous MEG spindles. Hum. Brain Mapp. 32, 2217–2227. https://doi.org/10.1002/hbm.21183

Dehghani, N., Cash, S.S., Rossetti, A.O., Chen, C.C., Halgren, E., 2010. Magnetoencephalography Demonstrates Multiple Asynchronous Generators During Human Sleep Spindles. J Neurophysiol 104, 179–188. https://doi.org/10.1152/jn.00198.2010

Delorme, A., Makeig, S., 2004. EEGLAB: an open source toolbox for analysis of single-trial EEG dynamics including independent component analysis. J. Neurosci. Methods 134, 9–21.

Destexhe, A., Contreras, D., Steriade, M., Sejnowski, T.J., Huguenard, J.R., 1996. In vivo, in vitro, and computational analysis of dendritic calcium currents in thalamic reticular neurons. J. Neurosci. 16, 169–85. https://doi.org/10.3961/jpmph.2008.41.6.365

Diekelmann, S., Born, J., 2010. The memory function of sleep. Nat. Rev. Neurosci. 11, 114–126. https://doi.org/10.1038/nrn2762

Einevoll, G.T., Kayser, C., Logothetis, N.K., Panzeri, S., 2013. Modelling and analysis of local field potentials for studying the function of cortical circuits. Nat. Rev. Neurosci. 14, 770–785. https://doi.org/10.1038/nrn3599

Fischl, B., 2012. FreeSurfer. Neuroimage. https://doi.org/10.1016/j.neuroimage.2012.01.021

Gramfort, A., Papadopoulo, T., Olivi, E., Clerc, M., 2010. OpenMEEG: opensource software for quasistatic bioelectromagnetics. Biomed. Eng. Online 9, 45. https://doi.org/10.1186/1475-925X-9-45

Hagler, D.J., Ulbert, I., Wittner, L., Eross, L., Madsen, J.R., Devinsky, O., Doyle, W., Fabo, D., Cash, S.S., Halgren, E., in press. Heterogeneous origins of human sleep spindles in different cortical layers. J. Neurosci. https://doi.org/10.1101/221234

Hämäläinen, M.S., Ilmoniemi, R.J., 1994. Interpreting magnetic fields of the brain: minimum norm estimates. Med. Biol. Eng. Comput. 32, 35–42. https://doi.org/10.1007/BF02512476

Herdin, M., Czink, N., Ozcelik, H., Bonek, E., 2005. Correlation matrix distance, a meaningful measure for evaluation of non-stationary MIMO channels. Veh. Technol. Conf. 2005. VTC 2005-Spring. 2005 IEEE 61st 1, 136–140 Vol. 1. https://doi.org/10.1109/VETECS.2005.1543265

Huguenard, J.R., McCormick, D.A., 1992. Simulation of the currents involved in rhythmic oscillations in thalamic relay neurons. J. Neurophysiol. 68, 1373–1383. https://doi.org/10.1017/CBO9781107415324.004

Huguenard, J.R., Prince, D.A., 1992. A novel T-type current underlies prolonged Ca2+-dependent burst firing in GABAergic neurons of rat thalamic reticular nucleus. J. Neurosci. 12, 3804–3817. https://doi.org/10.1007/s00401-013-1221-7

Iber, C., Ancoli-Israel, S., Chesson, A., Quan, S., 2007. The AASM Manual for the Scoring of Sleep and Associates Events: Rules, Terminology and Technical Specifications, Sleep (Rochester). https://doi.org/10.1002/ejoc.201200111

Irimia, A., Van Horn, J.D., Halgren, E., 2012. Source cancellation profiles of electroencephalography and magnetoencephalography. Neuroimage 59, 2464–2474. https://doi.org/10.1016/j.neuroimage.2011.08.104
Jones, E.G., 2002. Thalamic circuitry and thalamocortical synchrony. Philos. Trans. R. Soc. B Biol. Sci. 357, 1659–1673. https://doi.org/10.1098/rstb.2002.1168
Jones, E.G., 2001. The thalamic matrix and thalamocortical synchrony. Trends Neurosci. https://doi.org/10.1016/S0166-2236(00)01922-6
Komarov, M., Krishnan, G., Chauvette, S., Rulkov, N., Timofeev, I., Bazhenov, M., 2017. New class of reduced computationally efficient neuronal models for large-scale simulations of brain dynamics. J. Comput. Neurosci. 1–24. https://doi.org/10.1007/s10827-017-0663-7
Krishnan, G.P., Chauvette, S., Shamie, I., Soltani, S., Timofeev, I., Cash, S.S., Halgren, E., Bazhenov, M., 2016. Cellular and neurochemical basis of sleep stages in the thalamocortical network. Elife 5, 1–29. https://doi.org/10.7554/eLife.18607
Krishnan, G.P., Rosen, B.Q., Chen, J.-Y., Muller, L., Sejnowski, T.J., Cash, S.S., Halgren, E., Bazhenov, M., 2017. Thalamocortical and Intracortical Laminar Connectivity Determines Sleep Spindle Properties. bioRxiv 195552. https://doi.org/10.1101/195552
Linden, H., Tetzlaff, T., Potjans, T.C., Pettersen, K.H., Grun, S., Diesmann, M., Einevoll, G.T., 2011. Modeling the spatial reach of the LFP. Neuron 72, 859–872. https://doi.org/10.1016/j.neuron.2011.11.006
Lopes Da Silva, F., 2004. Functional localization of brain sources using EEG and/or MEG data: Volume conductor and source models, in: Magnetic Resonance Imaging. pp. 1533–1538. https://doi.org/10.1016/j.mri.2004.10.010
Lutkenhoner, B., 2003. Magnetoencephalography and its Achilles' heel, in: Journal of Physiology Paris. pp. 641–658. https://doi.org/10.1016/j.jphysparis.2004.01.020
McCormick, D.A., Pape, H.C., 1990. Properties of a hyperpolarization-activated cation current and its role in rhythmic oscillation in thalamic relay neurones. J. Physiol. 431, 291–318. https://doi.org/10.1113/jphysiol.1990.sp018331
Meyer, M., Desbrun, M., Schröder, P., Barr, A.H., 2003. Discrete Differential-Geometry Operators for Triangulated 2-Manifolds. pp. 35–57. https://doi.org/10.1007/978-3-662-05105-4_2
Nunez, P.L., Srinivasan, R., 2009. Electric Fields of the Brain: The neurophysics of EEG, Electric Fields of the Brain: The neurophysics of EEG. https://doi.org/10.1093/acprof:oso/9780195050387.001.0001
Oostenveld, R., Fries, P., Maris, E., Schoffelen, J.-M., 2011. FieldTrip: Open source software for advanced analysis of MEG, EEG, and invasive electrophysiological data. Comput. Intell. Neurosci. 2011, 156869. https://doi.org/10.1155/2011/156869
Pettersen, K.H., Devor, A., Ulbert, I., Dale, A.M., Einevoll, G.T., 2006. Current-source density estimation based on inversion of electrostatic forward solution: Effects of finite extent of neuronal activity and conductivity discontinuities. J. Neurosci. Methods 154, 116–133. https://doi.org/10.1016/j.jneumeth.2005.12.005
Piantoni, G., Halgren, E., Cash, S.S., 2016. Spatiotemporal Characteristics of Sleep Spindles Depend on Cortical Location. Neuroimage 146, 236–245. https://doi.org/10.1016/j.neuroimage.2016.11.010
Ritter, P., Schirner, M., McIntosh, A.R., Jirsa, V.K., 2013. The virtual brain integrates

computational modeling and multimodal neuroimaging. Brain Connect. 3, 121–145. https://doi.org/10.1089/brain.2012.0120
Rulkov, N.F., Timofeev, I., Bazhenov, M., 2004. Oscillations in Large-Scale Cortical Networks : Map-Based Model. J. Comput. Neurosci. 17, 203–223.
Rulkov, N.F., Bazhenov, M., 2008. Oscillations and synchrony in large-scale cortical network models. J. Biol. Phys. 34, 279–299. https://doi.org/10.1007/s10867-008-9079-y
Sejnowski, T.J., Destexhe, A., 2000. Why do we sleep? Brain Res. 886, 208–223. https://doi.org/10.1016/S0006-8993(00)03007-9
Smith, S.M., Beckmann, C.F., Andersson, J., Auerbach, E.J., Bijsterbosch, J., Douaud, G., Duff, E., Feinberg, D.A., Griffanti, L., Harms, M.P., Kelly, M., Laumann, T., Miller, K.L., Moeller, S., Petersen, S., Power, J., Salimi-Khorshidi, G., Snyder, A.Z., Vu, A.T., Woolrich, M.W., Xu, J., Yacoub, E., Uğurbil, K., Van Essen, D.C., Glasser, M.F., 2013. Resting-state fMRI in the Human Connectome Project. Neuroimage 80, 144–168. https://doi.org/10.1016/j.neuroimage.2013.05.039
Steriade, M., McCormick, D., Sejnowski, T., 1993. Thalamocortical oscillations in the sleeping and aroused brain. Science (80-.). 262, 679–685. https://doi.org/10.1126/science.8235588
Steriade, M., Timofeev, I., 2003. Review Neuronal Plasticity in Thalamocortical Networks during Sleep and Waking Oscillations present in the background electrical activity during the brain-activated states of waking and REM sleep, are also thought to enhance temporal coherence of re. Neuron 37, 563–576. https://doi.org/10.1016/S0896-6273(03)00065-5
Stevens, C.F., 1993. Quantal release of neurotransmitter and long-term potentiation. Cell. https://doi.org/10.1016/S0092-8674(05)80028-5
Timofeev, I., Grenier F., Bazhenov, M., Sejnowski, T.J., Steriade, M., 2000. Origin of Slow Cortical Oscillations in Deafferented Cortical Slabs. Cereb. Cortex 10, 1185–1199. https://doi.org/10.1093/cercor/10.12.1185
Ulbert, I., Halgren, E., Heit, G., Karmos, G., 2001. Multiple microelectrode-recording system for human intracortical applications. J. Neurosci. Methods 106, 69–79. https://doi.org/10.1016/S0165-0270(01)00330-2
van den Heuvel, M.P., Sporns, O., 2013. An Anatomical Substrate for Integration among Functional Networks in Human Cortex. J. Neurosci. 33, 14489–14500. https://doi.org/10.1523/JNEUROSCI.2128-13.2013

Tables

Table 1. Correlation matrix distances between empirical and simulated MEG/EEG covariance.

Subject	Core MEG	Matrix MEG	Core EEG	Matrix EEG
S1	0.285	0.312	0.17	0.0568
S2	0.668	0.685	0.125	0.115
S3	0.326	0.363	0.258	0.128

Figures and Legends

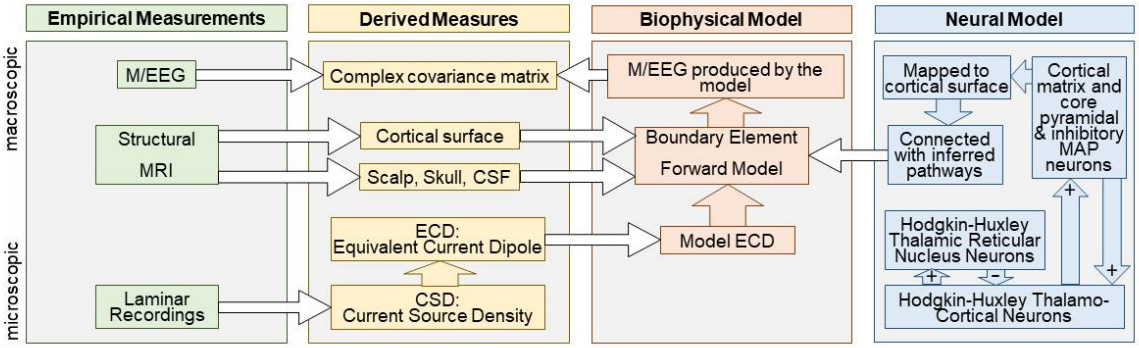

Fig. 1. Overall structure of Experiment.

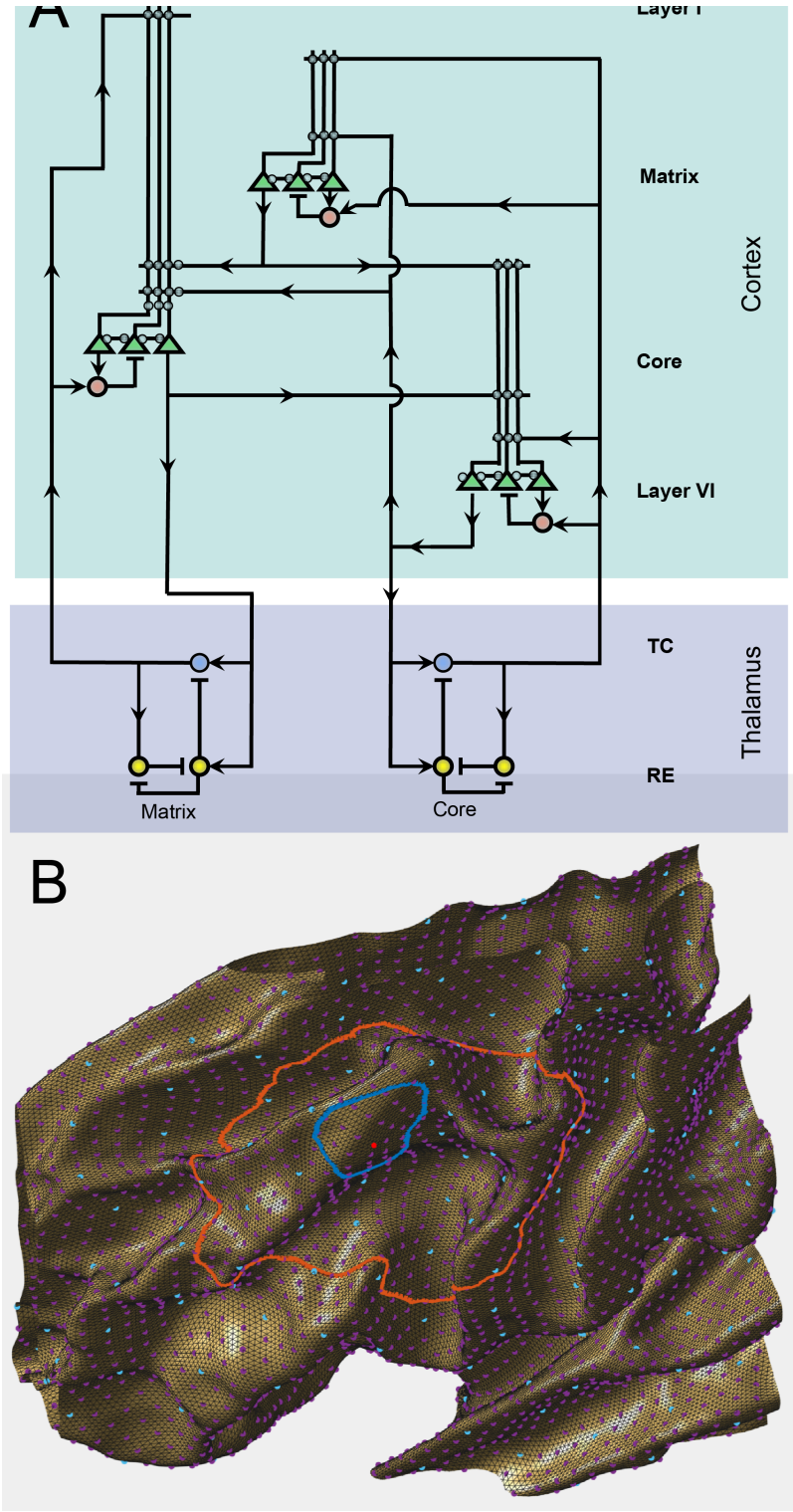

Figure 2. Network connectivity. (A) Schematic representation of thalamocortical and corticocortical connections. (B) Example of cortical geodesic-based connectivity. Pyramidal and inhibitory cortical neurons exist at purple and cyan locations, respectively. The blue contour shows the fanout of a core-projecting thalamic neuron at the virtual position marked in red. The orange contour shows the same for a matrix-projecting thalamic neuron at the same virtual location.

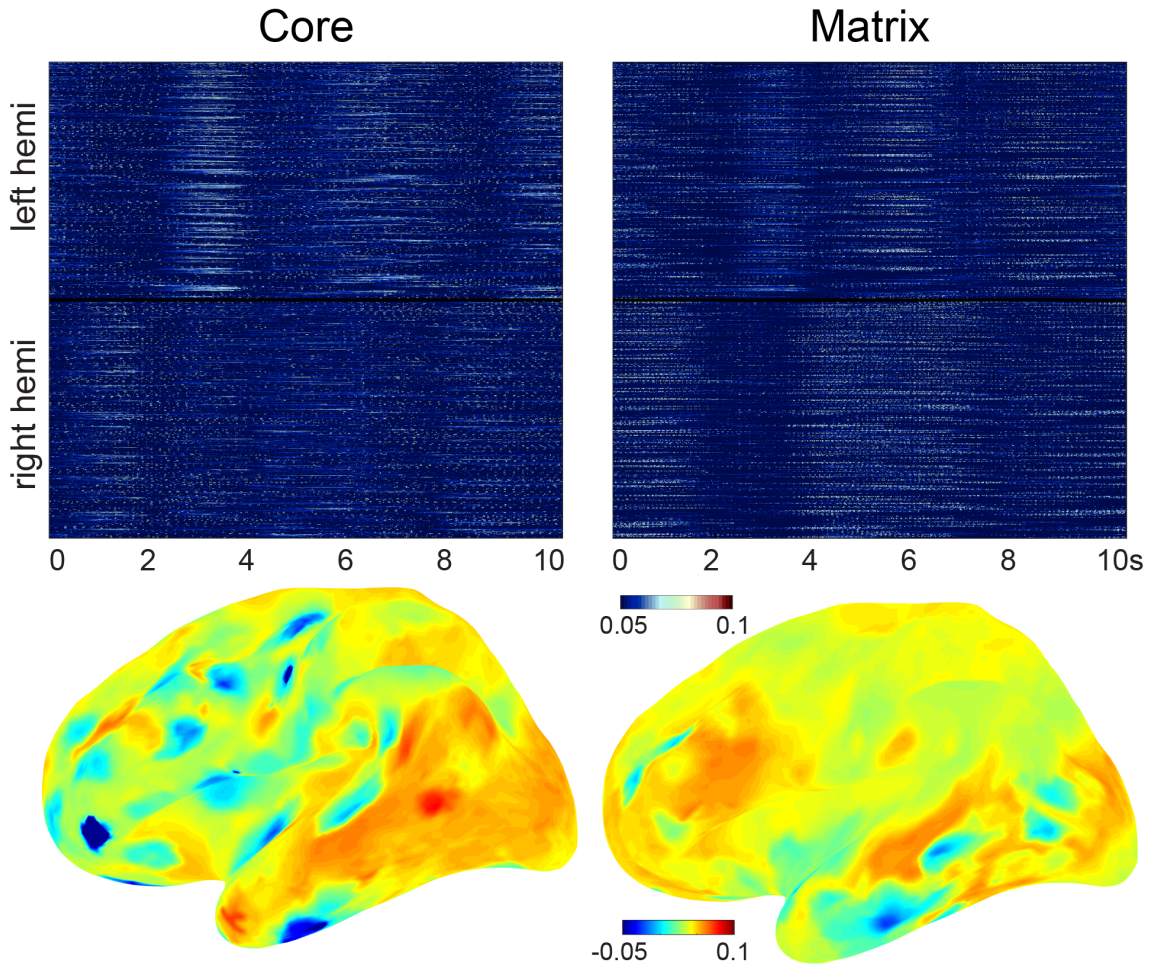

Figure 3. Simulated cortical sources. (A) 10 seconds of simulated N2 sleep for subject S1. (B) matrix and core pyramidal transmembrane currents distributed across the cortex at a single time point. Data are displayed on an inflated cortical surface.

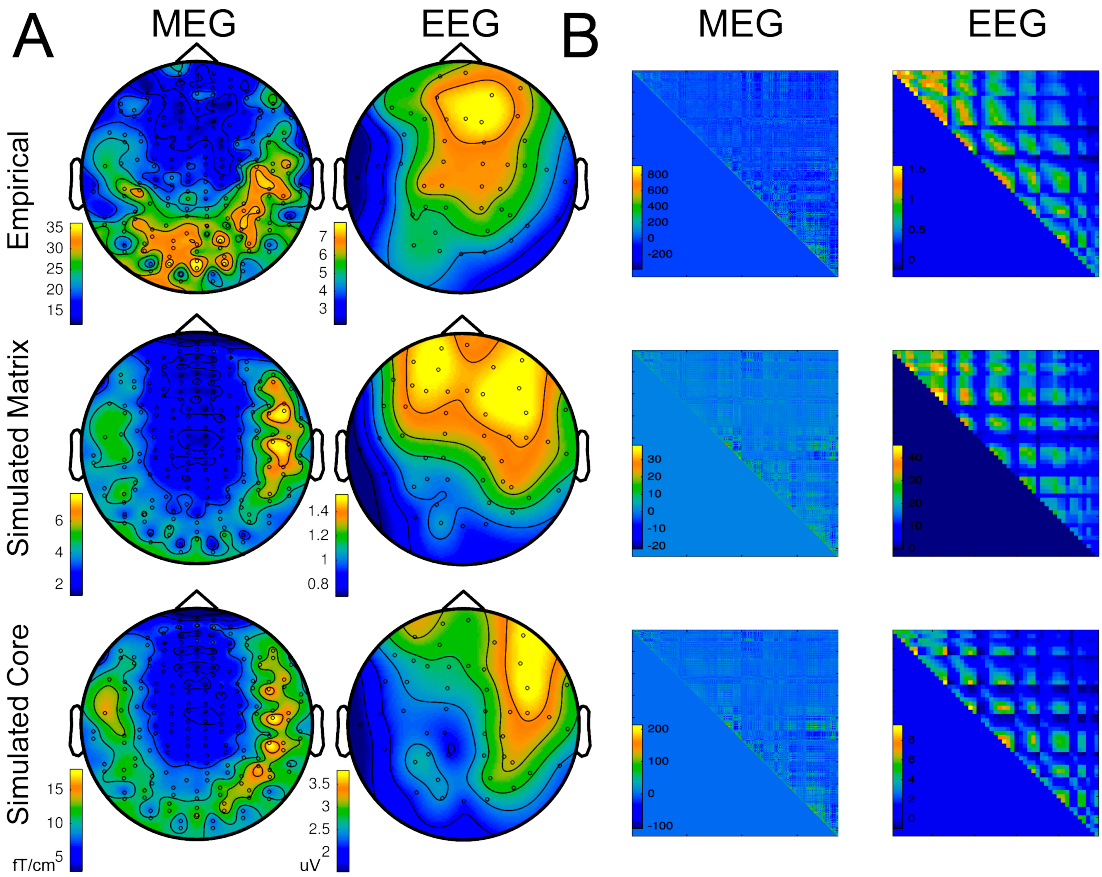

Figure 4. Empirical and Simulated MEEG sensors. (A) Average topographies and (B) variance-covariance matrices for empirical and simulated M/EEG. The matrix EEG and core MEG better match empirical amplitude and distribution than *vice versa*. Data shown summarize 10s of 10-16 Hz activity during N2 sleep for subject S1.